

Acoustic Interference Suppression in Ultrasound images for Real-Time HIFU Monitoring Using an Image-Based Latent Diffusion Model

Dejia Cai ^a, Yao Ran ^a, Kun Yang ^b, Xinwang Shi ^a, Yingying Zhou ^a, Kexian Wu ^a, Yang Xu ^{c,d}, Yi Hu ^{c,d},
Xiaowei Zhou ^{a,*}

^a State Key Laboratory of Ultrasound in Medicine and Engineering, College of Biomedical Engineering, Chongqing Medical University, Chongqing, 400016, China.

^b School of Microelectronics, Tianjin University, Tianjin, 300072, China

^c NMPA Key Laboratory for Quality Evaluation of Ultrasonic Surgical Equipment, Wuhan, 430075, China

^d Hubei Medical Devices Quality Supervision and Test Institute, Wuhan, 430075, China

*Correspondence:

Xiaowei Zhou

zhou.xiaowei@cqmu.edu.cn

Abstract

High-Intensity Focused Ultrasound (HIFU) is a non-invasive therapeutic technique widely used for treating various diseases. However, the success and safety of HIFU treatments depend on real-time monitoring, which is often hindered by interference when using ultrasound to guide HIFU treatment. To address these challenges, we developed HIFU-ILDiff, a novel deep learning-based approach leveraging latent diffusion models to suppress HIFU-induced interference in ultrasound images. The HIFU-ILDiff model employs a Vector Quantized Variational Autoencoder (VQ-VAE) to encode noisy ultrasound images into a lower-dimensional latent space, followed by a latent diffusion model that iteratively removes interference. The denoised latent vectors are then decoded to reconstruct high-resolution, interference-free ultrasound images. We constructed a comprehensive dataset comprising 18,872 image pairs from in vitro phantoms, ex vivo tissues, and in vivo animal across multiple imaging modalities and HIFU power levels to train and evaluate the model. Experimental results demonstrate that HIFU-ILDiff significantly outperforms the commonly used Notch Filter method, achieving a Structural Similarity Index (SSIM) of 0.796 ± 0.008 and Peak Signal-to-Noise Ratio (PSNR) of 23.780 ± 0.001 compared to SSIM of 0.443 and PSNR of 14.420 for the Notch Filter under in vitro scenarios. Additionally, HIFU-ILDiff achieves real-time processing at 15 frames per second, markedly faster than the Notch Filter's 5 seconds per frame. These findings indicate that HIFU-ILDiff is able to denoise HIFU interference in the ultrasound guiding images for real-time monitoring during HIFU therapy, which will greatly improve the treatment precision in current clinical applications.

Keywords: High-Intensity Focused Ultrasound, Real-Time Monitoring, High-Intensity Focused Ultrasound Interference Suppression, Latent Diffusion Model, Ultrasound Imaging, Non-invasive surgery

1.Introduction

High-intensity focused ultrasound (HIFU) is a non-invasive therapeutic technique extensively utilized for the treatment of various diseases, such as uterine fibroids [1] and breast fibroadenomas [2], with proven clinical efficacy. Compared to traditional surgical methods, HIFU offers benefits such as reduced recovery time, minimal tissue damage, and fewer complications. The success and safety of HIFU treatments hinge on real-time monitoring of the therapeutic process. Real-time monitoring is crucial to ensure the correct dosage of sonication at the target site and to prevent damage to surrounding healthy tissues. However, real-time and accurate monitoring of HIFU treatment remains the most significant challenge for this technology.

In clinical practice, both MRI and ultrasound imaging are used to guide and monitor HIFU procedures. MRI-guided HIFU (MRgHIFU) provides detailed temperature maps of the treatment area using the MRI thermography technique, making it the "gold standard" for monitoring. In fact, the MRI thermography can only get one frame of temperature map every 2-3 seconds during the HIFU sonication. However, the HIFU sonication could cause high dynamic biological effects within one second, or even down to tens of microseconds for the histotripsy treatment [3, 4], which is a subgroup of the HIFU. This means that MRI is unable to provide real-time HIFU monitoring. While ultrasound imaging has the potential offering real-time monitoring for HIFU treatment at a lower cost, it is underutilized due to mutual interference between the acoustic waves used for imaging and the treatment. More specifically, the strong acoustic waves from the HIFU transducer interfere with ultrasound imaging, contaminating signals acquired by the imaging transducer. To avoid this acoustic interference, the HIFU transducer is turned off during ultrasound imaging, leading to non-real-time monitoring and reduced treatment efficiency. Suppressing HIFU interference while maintaining real-time monitoring for ultrasound-guided HIFU treatment is crucial.

Recent years have seen a surge in efforts to suppress HIFU interference during ultrasound-guided treatments. The main goal is to develop real-time and effective algorithms which can get rid of the strong HIFU interference in the online ultrasound images and at the same time keep the guiding ultrasound images intact. For example, Yang et al. [5] introduced a frequency-domain robust principal component analysis (FRPCA) method to separate HIFU interference from contaminated B-mode images. Shen et al. [6] suggested using the Golay-encoded method to visualize imaged objects during simultaneous HIFU treatment. Similarly, Song et al. [7] developed an effective pulse sequence that minimizes interference between HIFU therapy and imaging. Shen et al. [8] employed Minimum-Peak-Sidelobe coded excitation to improve ultrasound imaging quality during concurrent HIFU treatment by suppressing sidelobe artifacts. Despite these advances, these signal processing methods were either too simple to have sufficient generalization when applied to different clinical scenarios, or too complicated to be used in real time. Payen et al. [9] proposed a novel passive elastography method for HIFU lesion detection to avoid direct interference with ultrasound imaging, but this too falls short in achieving real-time monitoring.

In contrast, deep learning methods have shown promising performance in suppressing HIFU interference. Lee et al. pioneered this approach with FUS-Net [10], a convolutional neural network that extracts "clean" ultrasound imaging data from RF data mixed with HIFU interference. Yang et al. [11] later improved upon this by suggesting that modeling based on one-dimensional RF data aligns better with the physical characteristics of RF data. However, their Unet-based networks lack robustness and generalization, performing well only in simple scenarios and struggling with more complex in vivo conditions. We considered the HIFU interference suppression as a high-resolution image reconstruction problem, treating RF data with interference as low-resolution images and clean RF data as high-resolution images [12]. This approach effectively suppressed interference, demonstrating superior robustness across various tissue types, even under higher irradiation intensities and in complex in vivo tissues.

Diffusion Probabilistic Models (DPMs) have achieved state-of-the-art performance in generative modeling,

excelling in density estimation and sample generation by effectively modeling complex data distributions [13, 14]. DPMs have shown strong results in image super-resolution [15, 16], and by adjusting reverse diffusion steps, they can generate high resolution ultrasound images tailored to clinical needs [12]. These strengths make DPMs promising for HIFU interference suppression. However, challenges remain, particularly slow inference and high computational costs when handling high-resolution images that require intensive gradient calculations. To address the limitation, Latent Diffusion Models (LDMs) [17] have emerged as an efficient alternative, operating within a compressed latent space to significantly reduce dimensionality and computational requirements. LDMs offer a promising approach by accelerating both training and inference times without compromising synthesis quality [18-20]. These advancements have opened new pathways for deploying DPMs in real-time applications, making them highly relevant to tasks such as HIFU interference suppression, where precision and efficiency are crucial.

Deep learning techniques indeed exhibit substantial superiority in removing the aforementioned acoustic interference for guiding and monitoring HIFU treatment. However, existing deep learning approaches predominantly concentrated on suppressing the HIFU interference based on the raw radiofrequency (RF) channel data, which is faced with several challenges: (1) large data volumes leading to increased model complexity and imperfect performance to meet the real-time requirement; (2) the heterogeneous nature of the RF datasets across various ultrasound imaging modalities necessitates the development of specific deep learning models tailored to each imaging modality, making existing deep learning methods not applicable to general scenarios. In this paper, we address the limitations of current deep learning models in suppressing strong HIFU interference for real-time guiding ultrasound images. We propose a novel approach that applies the diffusion model in latent space, rather than pixel space, and refer to this method as the **Image-based Latent Diffusion HIFU Interference Suppression Model (HIFU-ILDiff)**. Unlike previous methods that rely on raw RF data, our approach focuses directly on ultrasound images, which enhances both the efficiency and generalization of deep learning-based techniques. The primary contributions of this paper are summarized as follows:

- We introduced a latent space approach for HIFU interference suppression, reducing redundancy and noise while focusing on key features. This shift also lowers model complexity, accelerates training, and improves real-time inference.
- We proposed a novel image-based model for HIFU interference suppression, which addresses the real-time performance issues caused by previous RF data formats.
- We have constructed a large-scale HIFU interference suppression dataset with 18,872 image pairs, including data from in vitro phantoms, ex vivo, and in vivo tissues, across three typical imaging modes and four HIFU irradiation intensities, supporting the development of deep learning-based suppression methods.

2. Methods

2.1 Diffusion Model for Suppressing HIFU Interference in Ultrasound Images

To mitigate HIFU interference in ultrasound images, we apply a super-resolution (SR) reconstruction approach. SR is designed to enhance image resolution by recovering high-frequency details, making it effective for addressing the spatial degradation caused by HIFU interference. The HIFU interference often results in the loss of structural details in ultrasound images; however, SR reconstruction can restore these details by formulating the task as an inverse problem. Specifically, we estimate the high-resolution image x_H from the low-resolution image x_L through the following relationship:

$$x_L = D(x_H) + n$$

where D represents the downsampling operator modeling the interference, and n denotes the noise introduced

during the imaging process.

In our method, the diffusion model performs SR by iteratively refining the contaminated ultrasound image through a series of denoising steps. The forward process corrupts the high-resolution image by adding Gaussian noise:

$$q(x_t|x_{t-1}) = \mathcal{N}(x_t; \sqrt{\alpha_t}x_{t-1}, (1 - \alpha_t)\mathbf{I})$$

where x_t represents the image at time step t , and α_t is a noise scaling factor.

In the reverse process, the model begins with a random Gaussian distribution and progressively removes noise to reconstruct the clean high-resolution image. This denoising process is modeled by a neural network, which predicts the clean image's mean μ_θ and variance σ_θ at each step:

$$p_\theta(x_{t-1}|x_t) := \mathcal{N}(x_{t-1}; \mu_\theta(x_t, t), \sigma_\theta(x_t, t)^2 \mathbf{I})$$

This iterative denoising allows the model to suppress HIFU interference effectively while enhancing fine structural details. As a result, the diffusion-based SR reconstruction facilitates real-time guidance and monitoring of HIFU procedures, ensuring high-resolution, interference-free ultrasound imaging.

2.2 Super-resolution Images in Latent Space

In this study, we propose a latent diffusion model (LDM) for reconstructing high-resolution, interference-free ultrasound images within latent space. Unlike traditional methods that operate directly in the high-dimensional image space, we first map the noisy ultrasound images to a lower-dimensional latent space using a pretrained encoder. This encoding step serves to capture the essential features of the images, yielding a more compact and manipulable representation for subsequent interference suppression.

Once in the latent space, we use a diffusion model to iteratively refine the latent representation, suppressing the HIFU interference. The diffusion process involves progressively adding noise to the latent encoding during the forward pass and reversing this process during the generation phase to recover the clean latent vector. By conditioning the model on the noisy latent encoding, the diffusion model can focus specifically on removing interference while preserving the underlying tissue structures. Importantly, the model takes advantage of image-specific inductive biases to build the underlying UNet primarily from 2D convolutional layers, which allows for more efficient feature extraction and spatial representation in the latent space.

The objective of the diffusion model is further refined by focusing on the perceptually most relevant components of the image, using a reweighted bound that helps emphasize the preservation of essential tissue structures. This reweighted bound can be expressed as:

$$L_{LDM} := \mathbb{E}_{\xi(x), \epsilon \sim \mathcal{N}(0,1), t} [\|\epsilon - \epsilon_\theta(z_t, t)\|_2^2]$$

where $\epsilon_\theta(z_t, t)$ represents the neural network model to predict the denoised latent vector at each timestep t , and z_t is the noisy latent vector at timestep t . This formulation ensures that the model focuses on the most relevant features of the image while minimizing noise interference.

After the interference-free latent representation is obtained, a decoder is used to map it back into the image space, reconstructing the ultrasound image without HIFU interference. This indirect approach of working in the latent space before decoding enhances the stability and accuracy of the generated noise-free images, as it allows for better control over the suppression process.

2.3 Latent Diffusion Model Development

The proposed HIFU-ILDiff model leverages a latent diffusion framework for effective HIFU interference suppression and high-resolution image reconstruction in ultrasound imaging. As illustrated in Fig. 1, the model operates through two primary processes: forward training and reverse suppression of HIFU interference.

The forward training process unfolds in two stages. First, a VQ-VAE [21] model is trained to encode clean ultrasound images into a latent space. The encoder ξ of the VQ-VAE, along with the trainable encoder ψ for contaminated images, share an identical architecture, comprising two downsampling layers and a self-attention-enabled bottleneck layer. Each downsampling layer includes two ResNet blocks (without attention mechanisms) and a stride-2 convolutional layer for spatial downsampling, enabling efficient inference with minimal impact on accuracy. A vector quantization layer in the VQ-VAE discretizes the latent representations, while the decoder D reconstructs clean images, preserving essential structural features. After training the VQ-VAE, the parameters of ξ and D are frozen. The frozen encoder ξ encodes clean images into latent representations z , while ψ encodes contaminated images into a high-dimensional latent space. This alignment ensures dimensional consistency and structural coherence between the latent representations of clean and contaminated images. Subsequently, the trainable encoder ψ and a noise predictor $\hat{\epsilon}$ are optimized. The noise predictor, implemented as an attention-based U-Net, includes multiple ResNet blocks within both the encoder and decoder. Attention modules in specific layers enhance focus on areas affected by HIFU interference, improving noise estimation, while non-attention layers help maintain computational efficiency. The U-Net’s bottleneck attention layers capture long-range dependencies, reinforcing robustness across tissue types and interference levels.

During the forward diffusion process, Gaussian noise is incrementally added to latent representations. In the reverse diffusion process, conditioned on representations from ψ , the model gradually removes noise, reconstructing clean, high-resolution images. This alignment between clean and contaminated latent representations supports effective interference suppression and structural detail recovery.

The reverse sampling process uses the trained model for real-time HIFU interference suppression and image reconstruction. Contaminated images are encoded by ψ into latent space, conditioning the reverse diffusion process. Using the DDIM sampling approach, noise is progressively removed from the initial latent representation, refining it iteratively in each reverse step through the learned noise predictor $\hat{\epsilon}$. After denoising, the final clean latent representation is passed through the decoder D , reconstructing a high-resolution, interference-free image in pixel space. This diffusion-based method, integrated with the VQ-VAE encoder-decoder framework, enables efficient real-time reconstruction while preserving crucial diagnostic details.

In the reverse process, we utilize the Denoising Diffusion Implicit Model (DDIM) to accelerate inference and adapt to varying application requirements. Specifically, when real-time performance is a priority, a sampling step size of $K = 5$ can be employed, substantially enhancing inference speed while maintaining generation quality within the minimally acceptable range for practical applications. On the other hand, when the fidelity of generated sample details is critical, a larger sampling step size of $K = 30$ can be adopted. This setting enables the production of highly detailed and refined features while preserving a degree of real-time capability suitable for scenarios with moderate latency constraints. This adjustable sampling strategy ensures a flexible trade-off between inference speed and generation quality, thereby meeting diverse application demands.

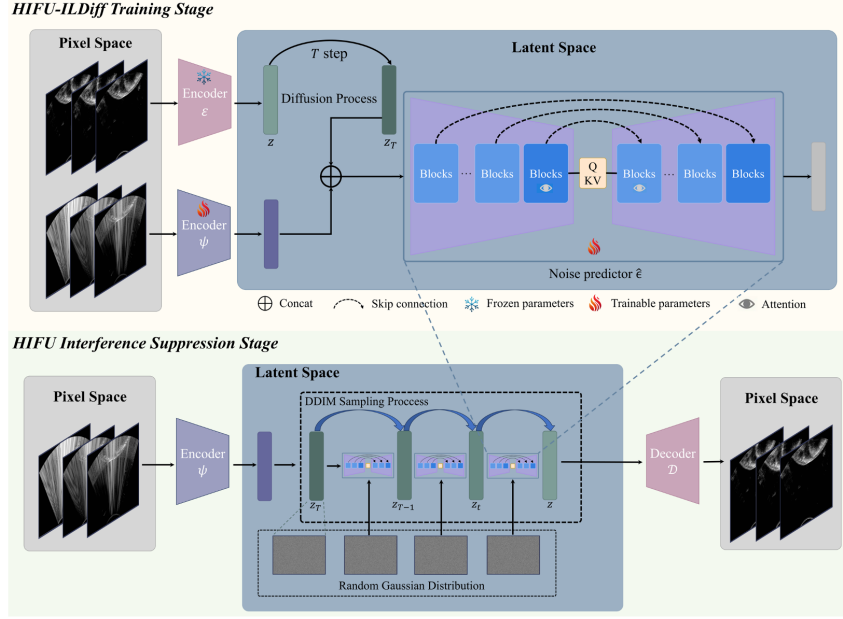


Fig. 1. The workflow and architecture of the HIFU-ILD Diff network for suppressing HIFU interference in imaging data.

2.4 Attention Mechanism for Enhanced Feature Learning

To improve feature learning for HIFU interference suppression, we incorporate a multi-head attention mechanism into our diffusion-based model. The network combines residual blocks for local feature learning with attention blocks, applied selectively at higher resolutions, to capture long-range dependencies, especially in regions impacted by HIFU interference.

The attention mechanism is implemented using the standard multi-head attention mechanism [22], which computes attention scores between query (Q), key (K), and value (V) matrices. The attention output is calculated as:

$$\text{Attention}(Q, K, V) = \text{Softmax}\left(\frac{QK^T}{\sqrt{d_k}}\right)V$$

This allows the model to focus on the most informative regions of the feature map, enabling it to capture long-range spatial dependencies and suppress irrelevant noise. The number of attention heads is dynamically determined based on the feature map's channel size, optimizing the allocation of attention across spatial regions.

By incorporating multi-head attention, the model can simultaneously focus on multiple regions of interest, improving its ability to recover high-resolution, interference-free ultrasound images. This approach enhances both the efficiency and accuracy of interference suppression while maintaining computational efficiency, ensuring that important structural details are preserved in the final image.

2.5 Experimental Setup and Data Acquisition

To acquire the experimental data, a clinically equivalent HIFU therapy system (Focused Ultrasound Tumor Therapeutic System, Model JC200, Chongqing Haifu Medical Technology Co., Ltd.) was used in conjunction with a Verasonics Vantage 256 ultrasound research platform (Verasonics Inc., USA) for ultrasound-guided HIFU procedures. A PC controlled a RIGOL DG4202 signal generator (RIGOL Technologies Co., Ltd.), which generated a continuous 0.97 MHz waveform. This signal was amplified through a power amplifier and transmitted via an electrical matching box to the HIFU transducer (Haifu, Chongqing, China) as shown in Fig. 2. The HIFU

transducer, with a central frequency of 0.97 MHz, had an outer diameter of 220 mm and an inner diameter of 80 mm, allowing it to accommodate the imaging transducer coaxially within its structure.

For ultrasound imaging, a consistent imaging depth of 135 mm-140 mm was maintained across all imaging techniques. Three imaging methods, commonly used in clinical settings, were implemented to evaluate the model's generalizability across different imaging approaches:

1. **Diverging Wave Compounding:** This method utilizes 11 angles, spanning from -20° to 20° , to create each compounded frame at a rate of 15 frames per second.
2. **Wide Beam Imaging:** In this mode, 48 rays were used to form each image, achieving a frame rate of 50 frames per second.
3. **Line Scan Imaging:** This technique employed 128 scan lines to generate each image frame at 15 frames per second, forming the final ultrasound image.

To simulate diverse HIFU treatment scenarios, four clinically relevant acoustic power levels—123W, 167W, 220W, and 277W—were applied. Each power level met the requirements for clinical HIFU applications, introducing varying degrees of HIFU interference that enriched the dataset and facilitated robust model validation across a range of treatment intensities.

The data collection was conducted over a continuous three-month period, with distinct datasets for training, testing, and validation sourced from different animals to improve the model's generalization capability. Variations in ambient conditions, such as temperature, were introduced naturally as data were acquired on different days, simulating real-world fluctuations encountered in clinical HIFU applications. This approach not only promotes the model's robustness and generalizability but also ensures that testing and validation protocols closely reflect clinical use scenarios.

Each HIFU transmission was activated for 200 milliseconds, followed by a 200-millisecond deactivation period, repeated over 25 cycles per session, as shown in Fig. 3. During each cycle, frames were captured in both HIFU-on and HIFU-off states to create labeled pairs for training, testing, and validation. Specifically, the last two frames with HIFU-on were paired with the immediately following frame with HIFU-off, generating two distinct labeled pairs per cycle. This process produced 50 pairs of images per experiment, each containing one frame with HIFU interference and its corresponding interference-free frame, thereby providing a comprehensive dataset for model training, testing, and validation in HIFU interference suppression.

To evaluate the model's performance in terms of resolution and contrast, a custom TMM (Tissue-Mimicking Material) phantom was constructed. During phantom preparation, two rigid plastic tubes, each with a diameter of 1 cm, were embedded within the TMM matrix as hollow channels. These tubes were later removed during imaging, leaving two empty spaces where no TMM material was present. This design provided a clear contrast between regions with and without phantom material, allowing us to assess the model's ability to suppress HIFU interference and verify that the reconstructed images accurately reflect the actual structure. Additionally, four symmetric holes were created on the top, bottom, left, and right sides of the phantom, each threaded with 0.1 mm thick fishing lines to form a cross pattern, further supporting evaluations of the model's resolution and contrast restoration capabilities.

The dataset for training, testing, and validation also included ex vivo samples, specifically pork loin, pork belly, beef heart, and beef liver, sourced locally. These tissues were selected because they closely resemble those commonly targeted in clinical HIFU treatment procedures. In vivo data was acquired from an anesthetized New Zealand rabbit, with heart and liver tissues as the primary focus. Target areas were shaved to enhance acoustic coupling.

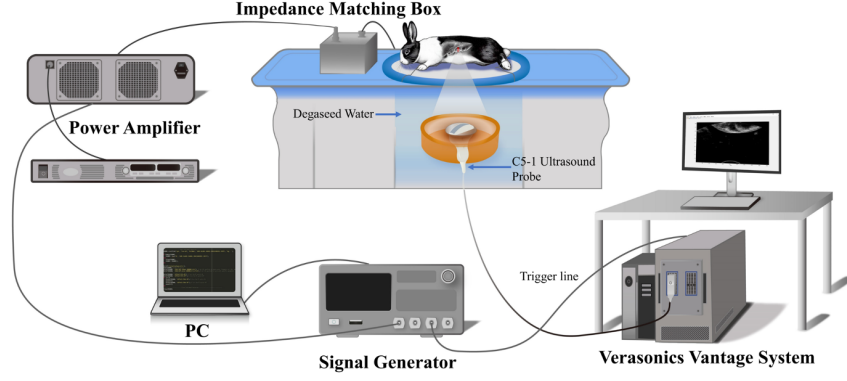


Fig. 2. Experimental setup for acquiring the HIFU interference dataset.

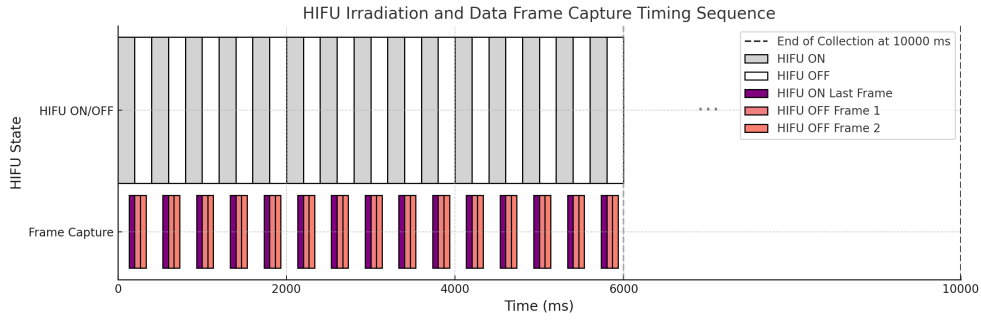


Fig. 3. Timing control diagram for ultrasound signal acquisition and HIFU switching.

2.6 Distribution of the Image-based Dataset

The dataset includes three commonly used clinical imaging modalities and four power levels typically employed in HIFU therapy, covering a variety of experimental subjects, including in vitro phantoms, ex vivo tissues, and in vivo tissues, as shown in Fig. 4. This diversity enables a comprehensive assessment of the model's capability in HIFU interference suppression. During data acquisition, we standardized the images generated from different imaging modalities to ensure a consistent image size of 512×512 pixels, with pixel values normalized to $[0, 1]$. Table 1 presents a detailed statistical distribution of the dataset's composition, which is ideally divided into three subsets: 60% for training, 20% for validation, and 20% for testing. After screening and filtering, we achieved an approximate data ratio close to the target proportions. Specifically, the dataset consists of 11,483 frames in the training set, 3,539 frames in the testing set, and 3,780 frames in the validation set, with a combined total of 18,802 frames. To ensure the independence and generalization capability of the dataset, this partitioning was implemented during the data collection phase, with each subset consisting of data from distinct experimental subjects or tissue samples. In addition to the training, testing, and validation sets, we collected a separate dataset comprising continuous HIFU interference frames. This dataset is designed to simulate the real-world HIFU treatment process.

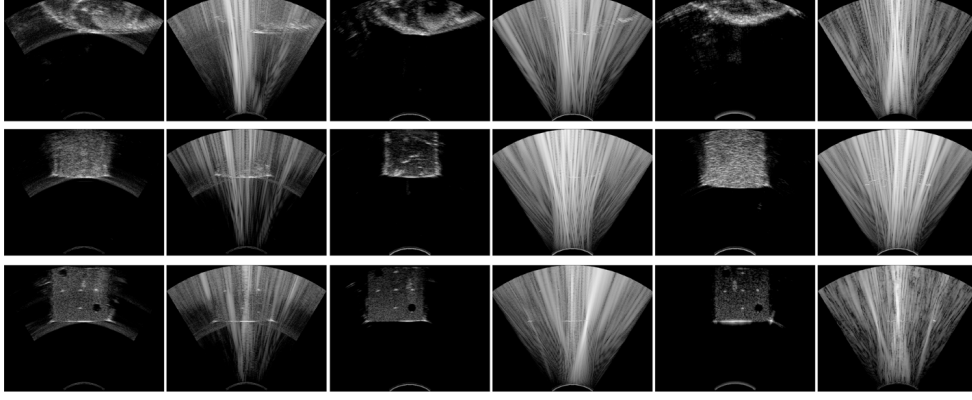


Fig. 4. Randomly selected B-mode images from the dataset with different tissue types and acoustic power levels. The top, middle, and bottom rows represent phantom, ex vivo, and in vivo tissues, respectively. Each row displays images from three imaging modalities (left to right), followed by corresponding images with HIFU interference

Table 1

Dataset Composition and Distribution.

Metric	Total Dataset	Training	Validation	Test
Phantom tissues	1,408	846	278	284
Ex vivo tissues	11,514	6,973	2,307	2,234
In vivo tissues	5,880	3,664	1,021	1,195
DW* imaging	6,131	3,771	1,209	1,151
WB* imaging	6,440	3,929	1,232	1,279
LS* imaging	6,231	3,783	1,292	1,156
APL* at 123W	5,098	3,091	1,001	1,006
APL* at 167W	4,304	2,612	868	824
APL* at 220W	5,368	3,355	1,020	993
APL* at 277W	4,032	2,425	891	716
Total	18,802	11,483	3,780	3,539

* The terms DW, WB, LS, and APL refer to Divergent Wave, Wide Beam, Line Scan, and Acoustic Power Level, respectively.

2.7 Model Implementation Details

The model training workflow begins with the VQ-VAE, configured with 64 base channels and channel multipliers [1,2,4]. The VQ-VAE has an embedding dimension of 3 and a codebook size of 8192, ensuring consistent and robust latent representations across diverse input variations. The VQ-VAE is first trained to convergence, establishing a stable latent space prior to training the diffusion model’s noise predictor. A custom loss function, integrating both perceptual and adversarial components, is applied to enhance perceptual fidelity, with a discriminator component to further refine the realism of reconstructions.

The diffusion model’s noise predictor $\hat{\epsilon}$, implemented as a self-attention-enabled U-Net, is configured with an initial 160 channels and channel multipliers [1,2,2,4]. Self-attention blocks within the U-Net are set with several attention head channels of 32, while a dropout rate of 0.3 is applied to improve generalization. The diffusion process spans 1000 timesteps, employing a linear noise schedule ranging from 0.0015 to 0.0155. These hyperparameters were determined through extensive tuning to optimize model performance.

Training is conducted on eight NVIDIA A100-SXM4-40GB GPUs. The VQ-VAE undergoes 1500 training steps with a learning rate of 4.5×10^{-6} , followed by 5500 steps for the diffusion model and noise predictor with a learning rate of 1.0×10^{-6} . The Adam optimizer [23], with a batch size of 3, is utilized to balance convergence

stability and memory efficiency. The final model parameters are selected based on the checkpoint achieving the best performance on the validation set during training, ensuring optimal results for subsequent evaluation. The entire model was trained continuously for approximately 7 days. Data preprocessing includes normalizing image pixels to $[0,1]$, along with random flipping and rotation to enhance the model's robustness across varying ultrasound imaging conditions.

2.8 Evaluation of the HIFU Interference Suppression

To evaluate the effectiveness of our proposed HIFU-ILDiff method, we compared it with the Notch Filter, a widely used signal processing technique for interference suppression [24-26]. The reason that no DL-based methods are chosen for comparisons is that existing DL methods rely on raw ultrasound imaging data and are very complicated to implement with such a large amount of data. The Notch Filter operates by selectively attenuating a specific frequency band corresponding to the HIFU interference, while leaving other frequencies largely unaffected. This approach is effective when the interference frequency is known and stable.

For quantitative evaluation, we used two widely recognized metrics: SSIM (Structural Similarity Index) [27] and PSNR (Peak Signal-to-Noise Ratio) [28]. SSIM measures the perceptual similarity between two images based on structural, luminance, and contrast information, with values ranging from 0 to 1, where 1 indicates perfect structural similarity. PSNR evaluates the signal-to-noise ratio, with higher values indicating less distortion. Ultrasound images collected while HIFU sonication was off were chosen as the reference while calculating the SSIM and PSNR values. These metrics were employed to assess the image quality of the denoised ultrasound images generated by HIFU-ILDiff and the Notch Filter, providing a comprehensive comparison of their performance.

3. Results

3.1. Visual inspection of the reconstructed images

As illustrated in Fig. 5, a comparative analysis was conducted between our method and the widely used Notch Filter across different B-mode imaging scenarios in the standard ultrasound imaging phantom under HIFU irradiation powers of 123 W and 220 W. The first column displays B-mode images acquired during HIFU therapy, where severe interference obscures nearly all tissue features. The second column presents Ground Truth (GT) images captured immediately after turning off the HIFU, serving as the reference. The third column demonstrates that the images reconstructed by the proposed method, successfully preserving critical details of different targets in the standard phantom when compared with the GT images. Notably, all images in the third column were generated with a sampling step size of $K = 30$ to achieve high reconstruction quality while maintaining good real-time performance. By comparison, the Notch Filter method, shown in the fourth column, failed to suppress interference effectively.

The performance was further evaluated across four power levels (123 W, 167 W, 220 W, and 277 W) under different imaging modes. Although the contaminated images exhibit significant HIFU interference, our model is able to reconstruct high-quality images with high consistency to their corresponding GT images, even at high power levels. Notably, the HIFU-ILDiff method removed most interference while accurately preserved the hyperechoic regions induced by HIFU therapy, which is important for the real-time monitoring of HIFU irradiation does. In contrast, the Notch Filter struggles to suppress the strong HIFU interference, producing blurred and distorted images. Fig. 6 demonstrates the model's adaptability across various types of ex-vivo tissue, including pork tenderloin, pork belly, beef liver, and beef heart. Our model effectively restores fine structural details, such as tissue textures and boundaries, even in challenging regions with high contrast, such as the fat layers in pork

belly and dense textures in beef heart. Conversely, the Notch Filter fails to remove interference adequately, resulting in incomplete artifact suppression and significant loss of structural details.

The proposed model's capability to suppress HIFU interference was also tested in vivo with HIFU irradiating at the rabbit's liver and heart tissues, as shown in Fig. 7. As in the in-vitro and ex-vivo situations, the HIFU-ILDiff model effectively removed the interference, restoring image quality to a level closely resembling the GT images. The Notch Filter once again failed to suppress interference adequately, leaving residual artifacts and distorting tissue features. The reconstructed images by the proposed method preserved critical anatomical details, such as liver lobule boundaries and cardiac muscle fibers. For different imaging modes, compared to divergent wave imaging, wide beam imaging and line-scan imaging exhibit higher spatial resolution but are more susceptible to stronger HIFU interference under the same HIFU power. By employing our proposed HIFU-ILDiff reconstruction method, the reconstructed images not only retain high spatial resolution but also accurately distinguish features across different imaging modes. This further demonstrates that our model possesses high robustness, strong generalization capability, and supports cross-mode compatibility. On the other hand, although the Notch filter can also be applied for HIFU interference suppression across different imaging modes, its inability to fully eliminate HIFU interference necessitates a reduction in spatial resolution, thereby limiting its effectiveness in high-resolution imaging applications.

Quality of the reconstructed images was evaluated by an experienced radiologist to assess the performance of the HIFU-ILDiff model. Image quality was classified into five levels according to Table 2, and the results are presented in Table 3. For sampling step $K = 30$, 33% of images were graded as excellent (Grade 5), 48% as good (Grade 4), and only 8% and 11% as poor (Grade 2) and fair (Grade 3), respectively, with no images deemed unacceptable (Grade 1). With $K = 5$, 18% of images were excellent, 55% good, 9% poor, and 18% fair, maintaining clinical utility. In contrast, the Notch Filter performed poorly, with 61% of images categorized as unacceptable and only 5% graded as good. These results highlight the HIFU-ILDiff model's ability to consistently produce qualified images, outperforming the conventional method.

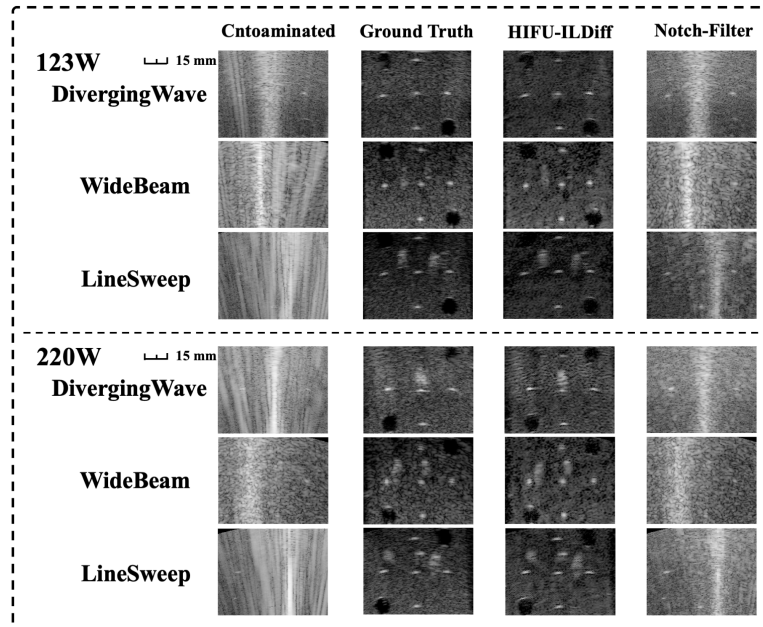


Fig. 5. Performance of HIFU interference suppression in in vitro phantom tissue at 123 W and 220 W across different imaging modalities. The first column shows B-mode images with HIFU interference. The second column shows B-mode images with HIFU off. The last two columns show B-mode images after applying different suppression methods.

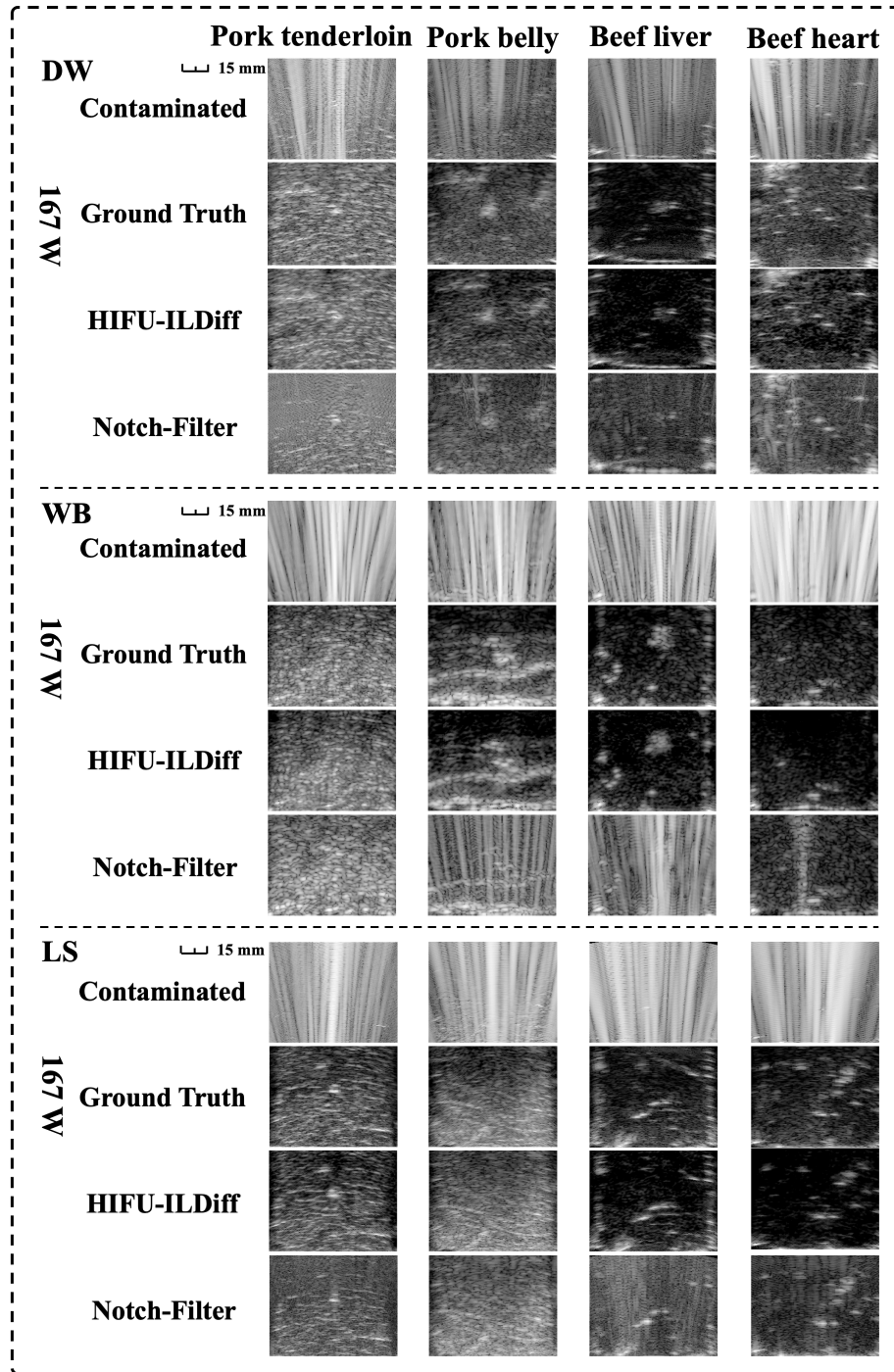


Fig. 6. Performance of HIFU interference suppression at 167 W irradiation power in different ex vivo tissues and imaging modalities. Each column represents a different tissue section. In each imaging modality, the first row shows B-mode images with HIFU interference, the second row shows B-mode images with HIFU off, and the last two rows show B-mode images after applying different suppression methods.

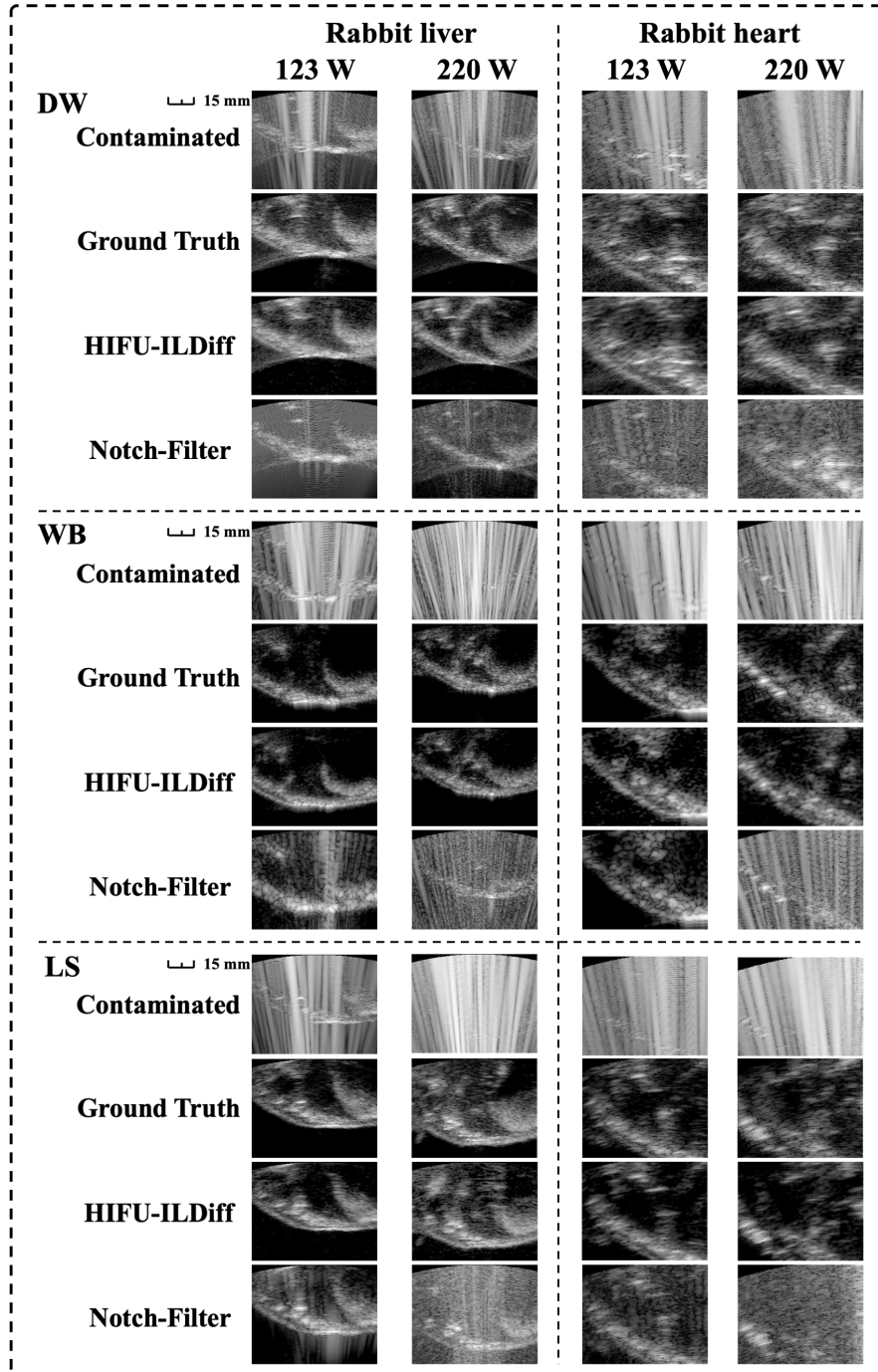


Fig. 7. Performance of HIFU interference suppression in different in vivo rabbit tissues at various HIFU irradiation powers and across different imaging modalities.

Table 2

Grading scale for subjective image analysis

Grade	Image Quality	Visibility of Anatomical Structures and Pathological Findings
5	Excellent image quality. High similarity to the reference image, with exceptional contrast	Excellent visibility of anatomical structures and pathological features, with sharp boundaries
4	Good image quality. Moderate similarity to ideal reference image, with good contrast.	Clear visibility of anatomical structures and features, with no restrictions for evaluation.
3	Fair image quality. Limited similarity to ideal reference image, with average contrast.	Partially blurred boundaries; limited visibility of anatomical structures and features.
2	Poor image quality. Low similarity to ideal reference image, with poor contrast.	Difficult to recognize anatomical structures; uncertain evaluation of pathological features.
1	Unacceptable image quality. Very low similarity to ideal reference image, with indistinguishable contrast.	Anatomical structures and pathological features are not discernible; diagnosis is impossible.

Table 3

Subjective evaluation of image quality

Methods	HIFU-ILDiff(K=30)	HIFU-ILDiff(K=5)	Notch-Filter
Image Quality			
5,excellent	394(33%)	215(18%)	0
4,good	574(48%)	657(55%)	60(5%)
3,fair	131(11%)	215(18%)	120(10%)
2,poor	96(8%)	108(9%)	287(24%)
1. unacceptable	0	0	728(61%)
Visibility			
5, excellent	657(55%)	502(42%)	0
4.clear	382(32%)	513(43%)	36(3%)
3.limited	96(8%)	120(10%)	179(15%)
2. poor	60(5%)	60(5%)	358(30%)
1. unacceptable	0	0	621(52%)

3.2. Quantitative Comparison

The quantitative performance of the HIFU-ILDiff model was evaluated using Structural Similarity Index (SSIM) and Peak Signal-to-Noise Ratio (PSNR) metrics, as summarized in Table 4 and illustrated in Fig. 8. In phantom experiments, the model with $K = 30$ achieved significantly higher SSIM (0.796 ± 0.008) and PSNR (23.780 ± 0.001) compared to the Notch Filter (SSIM: 0.443, PSNR: 14.420). A smaller sampling step size ($K = 5$) led to a slight reduction in image quality, but it provided faster inference and improved real-time imaging frame rates, making it suitable for time-sensitive applications. The confidence intervals (at a 0.95 confidence level) were estimated using the bootstrap sampling method, with 1000 random samples.

For ex vivo and in vivo experiments, the HIFU-ILDiff model maintained its high performance, achieving an SSIM of 0.801 ± 0.001 and PSNR of 24.562 ± 0.004 at $K = 30$. Even when the sampling step size was reduced to $K = 5$, the model consistently outperformed the Notch Filter, with SSIM and PSNR values higher than the latter (SSIM: 0.576, PSNR: 18.641). These results highlight the robustness of the proposed model across different tissue conditions, effectively suppressing interference while preserving structural details critical for diagnostic purposes.

The boxplots in Fig. 8(a)–8(d) provide a detailed comparison of the distributions for both phantom and tissue experiments. For both SSIM and PSNR metrics, the HIFU-ILDiff model with $K = 30$ showed the highest median

values and the narrowest interquartile ranges in all experimental conditions, indicating its stability and accuracy. When the sampling step $K = 5$, the median performance was slightly lower, but it also exhibited consistent results superior to the Notch Filter. Particularly in the phantom tissue scenarios (Fig. 8(a) and 8(b)), the Notch Filter demonstrated much lower and more dispersed metric values compared to our method.

Table 4

Quantitative comparisons of different methods

Methods	in vitro phantoms			
	<i>SSIM</i>	<i>SSIM CI (95%)</i>	<i>PSNR</i>	<i>PSNR CI (95%)</i>
HIFU-ILDiff(K=30)	0.796 ± 0.008	[0.791, 0.802]	23.780 ± 0.001	[23.671, 23.892]
HIFU-ILDiff(K=5)	0.743 ± 0.002	[0.737, 0.749]	23.443 ± 0.005	[23.332, 23.552]
Notch-Filter	0.443	[0.436, 0.450]	14.420	[14.174, 14.667]
Methods	ex-vivo and in-vivo			
	<i>SSIM</i>	<i>SSIM CI (95%)</i>	<i>PSNR</i>	<i>PSNR CI (95%)</i>
HIFU-ILDiff(K=30)	0.801 ± 0.001	[0.799, 0.802]	24.562 ± 0.004	[24.520, 24.599]
HIFU-ILDiff(K=5)	0.767 ± 0.001	[0.765, 0.768]	24.433 ± 0.009	[24.392, 24.472]
Notch-Filter	0.576	[0.570, 0.580]	18.641	[18.486, 18.807]

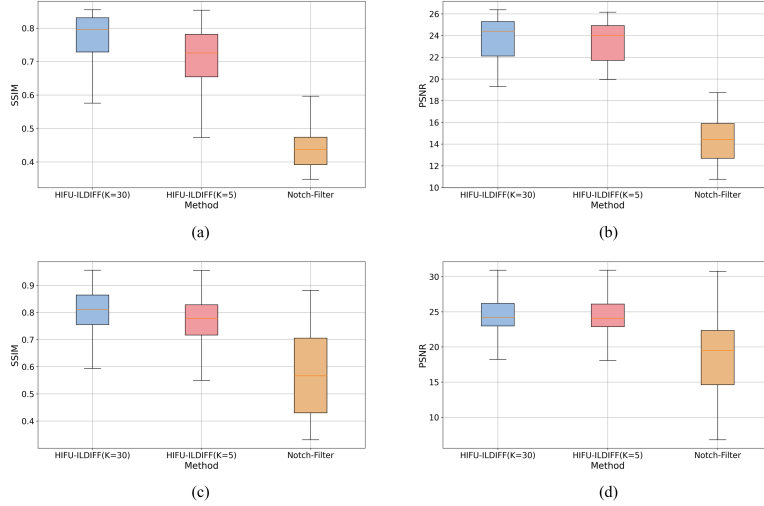


Fig. 8. Box plots comparing the results of different methods in terms of SSIM and PSNR. (a) and (b) show the results in the phantom model, while (c) and (d) display the results in ex vivo tissue.

3.3 Ablation study of proposed methods

In the ablation experiments, a fixed sampling step of $K = 30$ was used during the inference process. The experiments were conducted on both ex vivo and in vivo datasets to evaluate the impact of the diffusion step size T during the forward process, as well as the effect of applying the self-attention module at different stages on image quality after suppressing HIFU interference. As shown in Table 5, increasing the diffusion step size T considerably improves the quality of the generated images. However, when the step size reaches 2000, the image quality starts to degrade noticeably. Based on these findings, a diffusion step size of 1000 is identified as the optimal value for effectively suppressing HIFU interference while maintaining high-quality image generation.

Table 6 summarizes the results of the ablation study on the integration of the self-attention module, with checkmarks indicating configurations where the module was included. The introduction of the self-attention module into the VQ-VAE model led to a decline in the quality of the generated images, indicating that the self-attention mechanism may not perform effectively in the discrete latent space of the VQ-VAE. Conversely,

incorporating the self-attention module into the noise predictor substantially enhanced the quality of image generation while preserving real-time inference capability. This demonstrates that the self-attention mechanism effectively captures long-range dependencies without introducing substantial computational overhead. These findings highlight the importance of selectively integrating the self-attention module based on the task and the specific component of the model to achieve optimal performance.

Table 5

Ablation study of forward diffusion steps.

Diffusion Steps	SSIM	PSNR	Proportion of Good Image Quality
500	0.783	24.294	60%
1000	0.819	24.619	80%
2000	0.715	23.221	20%

Table 6

Ablation study on the effect of self-attention module integration.

Method	VQ-VAE	Noise-predictor	SSIM	PSNR	Inference Time (ms/frame)
1	✓	\	0.392	22.386	11
2	×	\	0.887	29.328	4
3	×	✓	0.819	24.619	342
4	×	×	0.769	23.991	330

3.4 Assessment of Real-Time Processing Efficiency

We measured the total time each method required to reconstruct a clear ultrasound image from a contaminated one. Unlike previous studies that predominantly focused on processing radiofrequency (RF) signals [10-12, 25], which often involve handling more than five sets of raw data to generate a single image frame, our proposed method achieves reconstruction through a single inference step. This streamlined approach substantially enhances processing efficiency. The inference times for each method are shown in Fig. 9, which clearly demonstrates that the proposed method in this study outperforms previous methods in terms of computational demand. Specifically, with the reduction in inference rounds, our method exhibits a significant time advantage. As illustrated in Fig. 11, the proposed HIFU-ILDiff methods, particularly with $K = 5$ and $K = 30$, demonstrate considerably faster inference times compared to other approaches. Specifically, the inference time for $K = 5$ is only 75 milliseconds, which is markedly lower than all other methods assessed. However, the traditional Notch-Filter method requires an inference time of 5 seconds, which is considerably longer and underscores its limitations in real-time performance, making it less suitable for applications demanding rapid processing.

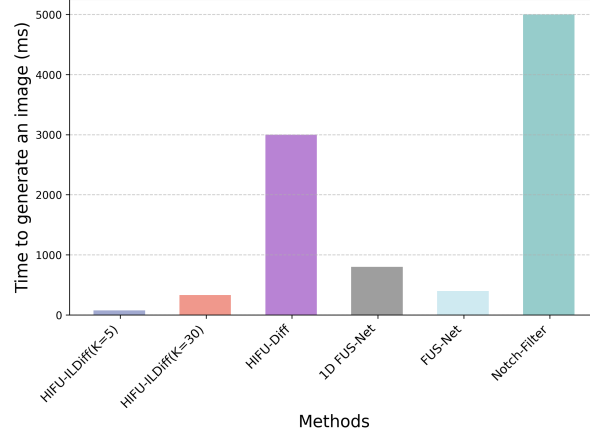


Fig. 9. Comparison of the time required for different methods in suppressing HIFU interference

3.5 HIFU interference-free images for ultrasound entropy imaging

To assess whether the image data generated by our proposed method retains the fundamental acoustic characteristics, we further validated the resultant image data with quantitative Weighted Ultrasound Entropy (WUE) imaging method [29]. WUE imaging works by applying weighted processing to the pixel intensity distribution of ultrasound images and calculating the entropy value, which quantifies the complexity and information content of the image. Fig. 10 shows the validation results for different imaging modes. The first column presents the B-mode images before HIFU interference suppression, which clearly exhibit interference artifacts, rendering them unsuitable for WUE imaging. The second column shows the B-mode images generated by our method after HIFU interference suppression. The third column displays the WUE imaging results applied to the data generated by our method. WUE imaging enables more accurate delineation of the boundaries between the treatment area and surrounding normal tissue, while markedly reducing noise interference. Overall, our experimental results indicate that the combination of our proposed method with ultrasound entropy imaging allows intraoperative real-time monitoring of the HIFU treatment.

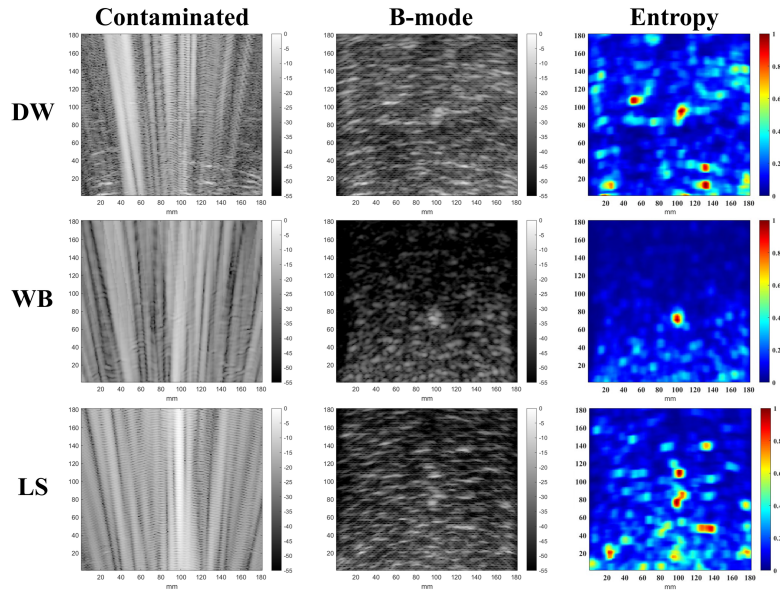


Fig. 10. Performance of the B-mode imaging algorithm and the quantitative weighted ultrasound entropy imaging algorithm across different imaging modalities.

4. Discussion

The continuous advancement of computing power has driven significant breakthroughs in artificial intelligence, particularly with the emergence of large generative models such as GPT [30, 31] and diffusion models [14, 32]. These models, trained on vast datasets and leveraging powerful computational resources, have achieved unprecedented accuracy and robustness in generative tasks. In this paper, we propose a HIFU interference suppression method based on a latent diffusion model, which aims to enhance the precision and efficiency of HIFU technology. Unlike existing methods which can only work with the raw imaging signals, the proposed method suppresses HIFU interference directly from ultrasound guiding images. Image-based interference suppression makes the method less demanding in computation and more robust for different ultrasound imaging algorithms. With the capability of removing HIFU interference in real time (up to 15 frames per second), the proposed method allows for more precise control of HIFU dosage and effectively mitigates the risk of over-treatment. A supplementary video demonstrates the practical effects of our model in a HIFU treatment scenario.

Inspired by the concept of super-resolution in computer vision, HIFU-ILDiff treats ultrasound images with HIFU interference as low-resolution images and their interference-free counterparts as high-resolution images. The model first encodes noisy ultrasound images into a latent space using a latent variable encoder, then conditions the diffusion model on this latent representation to control the stochasticity of the generation process. Instead of directly generating interference-free ultrasound images, our approach generates a corresponding latent vector, which is subsequently decoded back into the image space. This indirect approach significantly accelerating inference speed, while also improves the stability and accuracy of generated images, thereby enhancing real-time processing capability. Moreover, HIFU-ILDiff offers a trade-off between real-time performance and image quality through manual adjustment of the sampling step size K , making it adaptable to a wide range of clinical needs.

In our experiments, we constructed a large and comprehensive dataset to train and evaluate the generalization ability and robustness of our model. Fig. 5 to Fig. 7 demonstrate that the proposed method is broadly applicable for HIFU interference suppression across different imaging modalities, tissues, and HIFU power levels, with the reconstructed images showing high similarity to the Ground Truth (GT). Specifically, in the in vitro phantom experiments (Fig. 5), the ultrasound images generated by HIFU-ILDiff exhibit similar spatial resolution and contrast characteristics to the GT. In the in vivo experiments (Fig. 7), motion and respiratory effects caused additional variations between ultrasound frames, making it difficult to capture image details. Additionally, artifacts beyond HIFU interference were present. Despite these challenges, the interference-free ultrasound images reconstructed by HIFU-ILDiff accurately preserved the original details. This underscores the remarkable robustness of our approach. Collectively, these findings demonstrate that the HIFU-ILDiff model performs consistently and reliably across phantom, ex vivo, and in vivo conditions, offering a dependable solution for suppressing HIFU interference.

In the calculation of quantitative results, each outcome was generated from three randomly selected training parameters, with three random trials performed for each model configuration. As shown in Table 4, the variance in the reconstructed images across all datasets is consistently below 0.1, demonstrating the high stability of our model in both training and prediction. Although the SSIM and PSNR parameters indicate room for improvement, this method significantly outperforms traditional imaging signal-based methods in terms of real-time processing and image quality [10-12].

The ultrasound images denoised by HIFU-ILDiff retain the original acoustic properties, meaning that our model specifically suppresses HIFU interference without altering inherent characteristics of the ultrasound images. As shown in Fig. 10, when combined with quantitative ultrasound imaging, our approach facilitates more effective and intuitive detection of the HIFU focal point and associated tissue damage. This integration enhances the

precision and clarity in identifying subtle damage, such as thermal injury and necrosis at the early stage of HIFU sonication, which are critical for monitoring of HIFU treatment. Without the HIFU interference, the ultrasound guiding images can be better utilized to provide valuable insights into treatment progress, support informed decision-making, and ultimately contribute to improved treatment outcomes.

Despite its promising performance, HIFU-ILDiff has several limitations. Its effectiveness heavily relies on the quality and diversity of the training data, with performance potentially degrading when applied to unseen clinical data, such as data from different organs of human body. Moreover, the model assumes that HIFU interference can be effectively modeled as noise, but real-world interference may involve more complex and dynamic patterns that the current model might not fully capture. While HIFU-ILDiff allows for a trade-off between real-time performance and image quality by adjusting the sampling step size K , both its accuracy and real-time capability still require improvement. As shown in Table 3, although over 80% of the denoised images are rated as "good" or higher, less than 50% are classified as "excellent," highlighting potential for further improvement. Future work should focus on enhancing the robustness and adaptability of HIFU-ILDiff by incorporating more diverse datasets, addressing complex and dynamic interference patterns, refining the balance between real-time performance and image quality, and optimizing computational efficiency. Furthermore, it is essential to conduct clinical trials to validate the model's performance in clinical settings. Additionally, collection of clinical datasets will be necessary to assess generalizability of the method across different patients and a variety of clinical conditions.

The full source code for the HIFU-ILDiff model is publicly available at <https://github.com/caidejia/HIFU-ILDiff>. In addition, sample datasets for evaluation are provided, with more data available upon request.

5. Conclusion

In this paper, we introduced the HIFU-ILDiff, a novel image-based Latent Diffusion Model for real-time suppression of HIFU interference on ultrasound images. By leveraging latent space encoding and image super-resolution, HIFU-ILDiff had improved generalizability and real-time performance when compared to existing methods, making it more applicable to ultrasound-guided HIFU treatments. Our method demonstrated robust performance across various scenarios, including in vitro phantoms, ex vivo, and in vivo experiments, with the ability to denoise ultrasound images at up to 15 frames per second. While HIFU-ILDiff offers a promising solution for real-time monitoring of the HIFU treatment, it currently relies on high-quality training data and needs to be further validated in more complex, dynamic interference patterns.

Acknowledgement

The authors sincerely thank Mr. Xiaobo Gong, Mrs. Yaqing You, and Mr. Bing Zhao from the National Engineering Research Center for Ultrasound and Medicine for their assistance in integrating the clinical HIFU system with the research ultrasound imaging system. All animal procedures were approved by the Animal Experimentation Ethics Committee of Chongqing Medical University (Chongqing, China) Animal Center and adhered to the applicable guidelines. This work was supported by the National Natural Science Foundation of China (Grant No. 12304508), the Natural Science Foundation of Chongqing, China (Grant No. CSTB2022NSCQ-MSX0968).

Reference

- [1] Y.Y. Dou, L. Zhang, Y. Liu, M. He, Y.Z. Wang, Z.B. Wang, Long-term outcome and risk factors of reintervention after high intensity focused ultrasound ablation for uterine fibroids: a systematic review and meta-analysis, *International Journal of Hyperthermia*, 41 (2024).
- [2] S. Imankulov, T. Tuganbekov, A. Razbadauskas, Z. Seidagaliyeva, HIFU treatment for fibroadenoma - a clinical study at National Scientific Research Centre, Astana, Kazakhstan, *Journal of the Pakistan Medical Association*, 68 (2018) 1378-1380.
- [3] K.J. Pahk, S. Lee, P. G  lat, M.O. de Andrade, N. Saffari, The interaction of shockwaves with a vapour bubble in boiling histotripsy: The shock scattering effect, *Ultrasonics Sonochemistry*, 70 (2021).
- [4] M.F. Iqbal, M.A. Shafique, M. Abdur Raqib, T.K. Fadlalla Ahmad, A. Haseeb, A. M A Mhjoob, A. Raja, Histotripsy: an innovative approach for minimally invasive tumour and disease treatment, *Annals of medicine and surgery* (2012), 86 (2024) 2081-2087.
- [5] K. Yang, Q. Li, J. Xu, M.X. Tang, Z. Wang, P.H. Tsui, X. Zhou, Frequency-Domain Robust PCA for Real-Time Monitoring of HIFU Treatment, *IEEE Transactions on Medical Imaging*, 43 (2024) 3001-3012.
- [6] C.C. Shen, R.C. Lin, N.H. Wu, Golay-Encoded Ultrasound Monitoring of Simultaneous High-Intensity Focused Ultrasound Treatment: A Phantom Study, *Ieee Transactions on Ultrasonics Ferroelectrics and Frequency Control*, 69 (2022) 1370-1381.
- [7] J.H. Song, J.H. Chang, An Effective Pulse Sequence for Simultaneous HIFU Insonation and Monitoring, *Ieee Transactions on Ultrasonics Ferroelectrics and Frequency Control*, 61 (2014) 1580-1587.
- [8] C.C. Shen, N.H. Wu, Ultrasound monitoring of simultaneous High-Intensity focused ultrasound (HIFU) therapy using Minimum-Peak-Sidelobe coded excitation, *Ultrasonics*, 138 (2024).
- [9] T. Payen, S. Crouzet, N. Guillen, Y. Chen, J.Y. Chapelon, C. Lafon, S. Catheline, Passive Elastography for Clinical HIFU Lesion Detection, *IEEE Trans Med Imaging*, 43 (2024) 1594-1604.
- [10] S.A. Lee, E.E. Konofagou, FUS-Net: U-Net-Based FUS Interference Filtering, *IEEE Trans Med Imaging*, 41 (2022) 915-924.
- [11] K. Yang, Q. Li, H. Liu, Q. Zeng, D. Cai, J. Xu, Y. Zhou, P.H. Tsui, X. Zhou, Suppressing HIFU interference in ultrasound images using 1D U-Net-based neural networks, *Phys Med Biol*, 69 (2024).
- [12] D. Cai, K. Yang, X. Liu, J. Xu, Y. Ran, Y. Xu, X. Zhou, Suppressing the HIFU interference in ultrasound guiding images with a diffusion-based deep learning model, *Computer Methods and Programs in Biomedicine*, (2024) 108304.
- [13] J. Ho, A. Jain, P. Abbeel, Denoising Diffusion Probabilistic Models, (2020).
- [14] P. Dhariwal, A. Nichol, Diffusion models beat GANs on image synthesis, *Proceedings of the 35th International Conference on Neural Information Processing Systems*, Curran Associates Inc., 2024, pp. Article 672.
- [15] C. Saharia, J.A.T. Ho, W.L. Chan, T. Salimans, D.J. Fleet, M. Norouzi, Image Super-Resolution via Iterative Refinement, *Ieee Transactions on Pattern Analysis and Machine Intelligence*, 45 (2023) 4713-4726.
- [16] A.X. Niu, T.X. Pham, K. Zhang, J.Q. Sun, Y. Zhu, Q.S. Yan, I.S. Kweon, Y.N. Zhang, ACDMSR: Accelerated Conditional Diffusion Models for Single Image Super-Resolution, *Ieee Transactions on Broadcasting*, 70 (2024) 492-504.
- [17] R. Rombach, A. Blattmann, D. Lorenz, P. Esser, B. Ommer, High-Resolution Image Synthesis with Latent Diffusion Models, *2022 IEEE/CVF Conference on Computer Vision and Pattern Recognition (CVPR)*, (2021) 10674-10685.
- [18] P. Esser, R. Rombach, B. Ommer, Taming Transformers for High-Resolution Image Synthesis, *2021 IEEE/CVF Conference on Computer Vision and Pattern Recognition (CVPR)*, 2021, pp. 12868-12878.

- [19] K. Zhang, J. Liang, L.V. Gool, R. Timofte, Designing a Practical Degradation Model for Deep Blind Image Super-Resolution, 2021 IEEE/CVF International Conference on Computer Vision (ICCV), 2021, pp. 4771-4780.
- [20] K. Zhao, K. Pang, A.L.Y. Hung, H. Zheng, R. Yan, K. Sung, MRI Super-Resolution with Partial Diffusion Models, IEEE transactions on medical imaging, PP (2024).
- [21] A. Razavi, A.v.d. Oord, O. Vinyals, Generating diverse high-fidelity images with VQ-VAE-2, Proceedings of the 33rd International Conference on Neural Information Processing Systems, Curran Associates Inc.2019, pp. Article 1331.
- [22] A. Vaswani, N.M. Shazeer, N. Parmar, J. Uszkoreit, L. Jones, A.N. Gomez, L. Kaiser, I. Polosukhin, Attention is All you Need, Neural Information Processing Systems, 2017.
- [23] D.P. Kingma, J. Ba, Adam: A Method for Stochastic Optimization, 2015.
- [24] J.S. Jeong, J.H. Chang, K.K. Shung, Pulse compression technique for simultaneous HIFU surgery and ultrasonic imaging: A preliminary study, Ultrasonics, 52 (2012) 730-739.
- [25] J.S. Jeong, J.M. Cannata, K.K. Shung, Adaptive HIFU noise cancellation for simultaneous therapy and imaging using an integrated HIFU/imaging transducer, Physics in Medicine and Biology, 55 (2010) 1889-1902.
- [26] J.S. Jeong, J.H. Chang, K.K. Shung, Ultrasound Transducer and System for Real-Time Simultaneous Therapy and Diagnosis for Noninvasive Surgery of Prostate Tissue, Ieee Transactions on Ultrasonics Ferroelectrics and Frequency Control, 56 (2009) 1913-1922.
- [27] K. Egiazarian, J. Astola, N. Ponomarenko, V. Lukin, F. Battisti, M. Carli, New full-reference quality metrics based on HVS, Proceedings of the second international workshop on video processing and quality metrics, 2006, pp. 4.
- [28] W. Zhou, A.C. Bovik, H.R. Sheikh, E.P. Simoncelli, Image quality assessment: from error visibility to structural similarity, IEEE Transactions on Image Processing, 13 (2004) 600-612.
- [29] Y. Zhou, K. Yang, J. Xu, D. Cai, X. Zhou, Weighted ultrasound entropy imaging for HIFU ablation monitoring with improved sensitivity and contrast, Medical Physics, 51 (2024) 8247-8259.
- [30] T.B. Brown, B. Mann, N. Ryder, M. Subbiah, J. Kaplan, P. Dhariwal, A. Neelakantan, P. Shyam, G. Sastry, A. Askell, S. Agarwal, A. Herbert-Voss, G. Krueger, T. Henighan, R. Child, A. Ramesh, D.M. Ziegler, J. Wu, C. Winter, C. Hesse, M. Chen, E. Sigler, M. Litwin, S. Gray, B. Chess, J. Clark, C. Berner, S. McCandlish, A. Radford, I. Sutskever, D. Amodei, Language models are few-shot learners, Proceedings of the 34th International Conference on Neural Information Processing Systems, Curran Associates Inc., Vancouver, BC, Canada, 2020, pp. Article 159.
- [31] W.X. Zhao, K. Zhou, J. Li, T. Tang, X. Wang, Y. Hou, Y. Min, B. Zhang, J. Zhang, Z. Dong, Y. Du, C. Yang, Y. Chen, Z. Chen, J. Jiang, R. Ren, Y. Li, X. Tang, Z. Liu, P. Liu, J. Nie, J.-r. Wen, A Survey of Large Language Models, ArXiv, abs/2303.18223 (2023).
- [32] L. Zhang, A. Rao, M. Agrawala, Adding Conditional Control to Text-to-Image Diffusion Models, 2023 IEEE/CVF International Conference on Computer Vision (ICCV), 2023, pp. 3813-3824.